FEDSM2024-130661

A COMPUTATIONAL ANALYSIS OF FLUID-STRUCTURE INTERACTION IN METACHRONAL PROPULSION

Zhipeng Lou¹, Menglong Lei¹, Margaret L. Byron², Chengyu Li¹

¹ Villanova University, Villanova, PA 19085, USA

² Pennsylvania State University, University Park, PA 16802, USA

ABSTRACT

Ctenophores employ flexible rows of appendages called ctenes that form the metachronal beating pattern. A complete cycle of such paddling consists of a power stroke that strokes backward to produce propulsion and a recovery stroke that allows the appendage to recover its initial position. Effective locomotion in these creatures relies on maximizing propulsion during the power stroke while minimizing drag in the recovery stroke. *Unlike rigid oars, the ctenes are flexible during both the power* stroke and the recovery stroke, and notably, their strokes are asymmetric, with faster movement during the power stroke. As previous research assumed uniform material properties. This assumption will eventually make the ctene deform more intensively in the power stroke than the recovery stroke due to the asymmetrical hydrodynamic forces. However, observations contradict these assumptions. One explanation posits that ctenes stiffen during the power stroke, enhancing their propulsive force, and become more flexible in the recovery stroke, reducing drag by minimizing the water-countering area. This study focusses on the influence of asymmetric stiffness on their propulsion mechanism. Inspired by nature, we conducted three-dimensional fluid-structure interaction (FSI) using an inhouse immersed-boundary-method-based flow solver integrated with a nonlinear finite-element solid-mechanics solver. This integrated solver uses a two-way coupling that ensures a higher accuracy regarding the complexity due to the involvement of the multiple ctenes in a ctene row. The preliminary results show that the anisotropic stiffness of the ctene have better accuracy of deformation as compared to the deformation recorded by the

high-speed camera. The asymmetric properties of the ctene material allow both the spatial and temporal asymmetry of the ctene beating pattern. Our investigation suggests that while symmetrical beating can only generate negative net thrust, a slightly asymmetrical beating can make the thrust positive. We find that power stroke period that cost 30% whole period can generates the highest thrust. As multiple ctenes involves, the interaction among ctenes can amplified the effects of the asymmetrical beating, so that the thrust generation is enhanced by 9 to 13 times because of it.

NOMENCLATURE

| OMENOLATORE | |
|----------------------------------|--------------------------|
| F_{T} | Thrust force |
| F_L | Lift force |
| C_T | Thrust coefficient |
| C_L | Thrust coefficient |
| C_p | Thrust coefficient |
| η | Power efficiency |
| $ar{U}_{\scriptscriptstyle tip}$ | Mean ctenes tip velocity |
| L | Ctene length |
| f | Flapping frequency |
| Re | Reynolds number |
| u_{i} | Velocity component |

p Pressure

v Seawater kinematic viscosity

T One cycle period

1. INTRODUCTION

Metachronal waves are commonly found among small swimming organisms which are equipped with cilia, pleopods, or other swimming appendages (e.g., paramecium, ctenophores, copepods, krill, and shrimp) [1,2]. Using a drag-based propulsion strategy, the closely spaced appendages sequentially execute a power stroke followed by a recovery stroke to generate fluid momentum in the opposite direction of animal motion. Two key features of metachronal paddling are the phase lag between adjacent appendages and the spatiotemporally asymmetric locomotion of individual appendages [3,4]. Specifically, the appendages interact with each other and are stimulated by their neighboring appendages sequentially, forming a metachronal wave. The observed spatiotemporal asymmetry may be the result of both fluid-structure interactions and possible stiffness differences between the power stroke and the recovery stroke. Propulsion is achieved during the power stroke, when the appendage beats opposite to the swimming direction. In general, the period of power stroke is shorter than that of the recovery stroke, which creates a temporal asymmetry during each beating cycle[4].

Most species using metachronal propulsion operate at the micron or millimeter scale. In the time-reversible flow regime (Re<1), a spatially asymmetric stroke is necessary to produce net fluid displacement[5]. In addition, the phase lag between adjacent appendages also plays an important role in driving flow [6]. At low-to-intermediate Reynolds numbers (10⁰<Re<10²), however, the level of spatiotemporal asymmetry may vary significantly. Herrera et al. experimentally measured the spatial and temporal asymmetry of ctenophores' propulsive strokes across a wide range of Reynolds numbers (Re≈20~200) [7]. Their results indicated that the level of spatial asymmetry decreases with the increasing Reynolds number, while the temporal asymmetry is more pronounced at higher Reynolds numbers. The ctenophore is also a typical metachronal swimmer who is equipped with multiple rows of appendages. Those appendages are also called comb-plates or ctenes which are some semi-fused ciliary structures that fuses on the substrate (Figure 1).

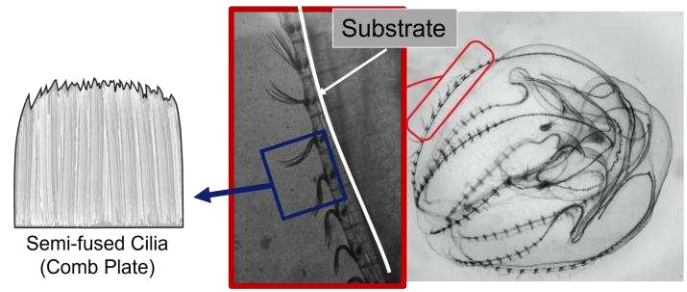


Figure 1. Illustration of the metachronal swimming of a ctenophore.

In our study, we have integrated our in-house computational fluid dynamics (CFD) solver with a finite element method (FEM) solver to solve fluid structure interaction problems. Convergence is achieved by strong coupling methods to generate more accurate solutions. The model of the appendages is constructed based on the structure of ctenophore to represent similar metachronal swimmers. Although many experimental studies have been demonstrated that the asymmetrical beating and interaction among multiple ctenes can enhance the hydrodynamic performance of metachronal swimming, they have limitation of choosing how much the asymmetry is. Thus, the results from the most studies are limited by the sample size. Other numerical studies that reconstructed models using real animals' data are also limited by the same reason. However, our FSI solver is capable of solving the problems for different kinematic but returns solution with higher fidelity as the deformation of real animals.

2. METHODOLOGY

2.1 3D modeling

In this study, a thin rectangular plate is used to represent the appendages of metachronal-swimming animals. The length and the width of the plates are denoted as L and W. The aspect ratio AR is 0.67 which is defined by AR=W/L as shown in figure 2. In the simulations of our study, the W and L are 0.8 and 1.2. The flow solver treats the plate as a membrane with no thickness, while the FEA solid solver treats the plates as a rectangular cuboid with thickness of 0.03.

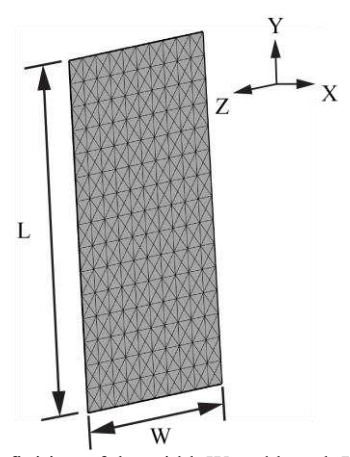


Figure 2. The definition of the width W and length L of the model.

2.3 Kinematics

The flat plate is given a rotation along its shorter side as shown in figure 3. The rotational kinematics is governed by the equation:

$$\Phi = \begin{cases} \frac{A}{2}cos(2\pi ft/(1-Ta)), & t = [0, t_p] \\ \frac{A}{2}cos(2\pi f(t+Ta)/(1+Ta)), & t = [t_p, T] \end{cases}$$
(1)

where Φ is the angle between the plate and the horizontal plane, A is the stroke amplitude, f is the beating frequency, Ta is the temporal asymmetry parameter, t_p is the power stroke duration. T is a full stroke period. Ta is used to determine the difference between power stroke duration t_p and recovery stroke duration t_r , which is defined as the equation [8]:

$$Ta = \frac{t_r - t_p}{t_r + t_p} \tag{2}$$

As Ta is 0, t_r equals to t_p which indicates this is a symmetrical beating. As Ta is set to larger than 0 but less than 1, the power stroke period is shorter than the recovery stroke period. The effects of the temporal asymmetry of the beating under different Reynolds number has been studied in our previous work, both numerically and experimentally[7,9]. The previous works are based on the data of real experiments. But the current work focuses on getting insight from a parametric study based on fluid structure interaction. The study has more control on the parameters on the kinematics without the limitation of the data sampling size from the experiments. For example, we can use any reasonable Ta to examine the kinematic while it is hard to control it of the real animals in the experiments.

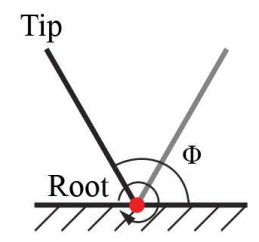


Figure 3. The definition of kinematics of the flat plate.

2.4 Fluid structure interaction solver

This study integrated our in house computation fluid dynamic (CFD) solver with an finite element method (FEM) solver (Vega FEM, University of Southern California, Los Angeles, CA) [10]. In each time step, as shown in **figure 4**, the CFD solver is strong coupled with the FEM solver. Similar coupling methods have been successfully adopted by studies for fish swimming and insect flight[11].

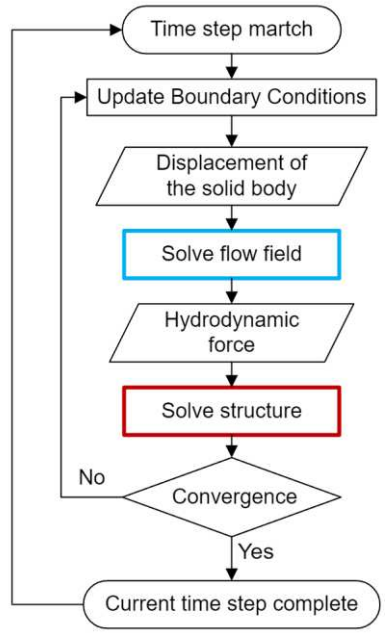


Figure 4. The definition of the width W and length L of the model.

2.5 Governing equations and numerical method for the flow

The governing equations adopted here are the unsteady incompressible viscous Navier-Stokes equations, which are shown in equation (2), and discretized using the collocated grid arrangement, where the primitive variables (u_i and p) are stored in the cell center.

$$\frac{\partial u_i}{\partial x_i} = 0 ; (3)$$

$$\frac{\partial u_i}{\partial t} + \frac{\partial (u_i u_j)}{\partial x_j} = -\frac{\partial p}{\partial x_i} + \frac{1}{Re} \frac{\partial}{\partial x_j} (\frac{\partial u_i}{\partial x_j})$$
(4)

where u_i (i = 1,2,3) are the velocity components in the x-, y-, and z-directions, respectively; p is the pressure, and Re is the Reynolds number. The oscillatory Reynolds number is used for this study, which is given by $Re_{\omega}=2\pi f L_{cilia}^2/v$.

The above equations are solved by a finite difference-based immersed-boundary method in a non-body-conforming Cartesian grid, which are integrated in time using the fractional step method. The advantage of the immersed-boundary method is that it is not necessary to use complicated re-meshing algorithms that are used by other conventional body conformal methods. Details of the CFD solver in solving the Navier–Stokes equations are elaborated and validated in our previous studies.

2.6 Validation

The conducted the validation by comparing the results of our solver with the results from Dai et al and Liu et al [12,13]. In the simulation for the validation, a flat plate was given a rotation along its leading edge as shown in figure 5, where the rotational kinematics is given by the equation:

$$\alpha = \alpha_0 \sin(2\pi f t) \tag{5}$$

where α_0 is the rotation amplitude which is 12°, f is the stroke frequency, t is the current time.

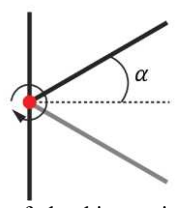


Figure 5. The definition of the kinematics from side view in the validation cases

To validate our solver, 5 simulations have been conducted under different reduced stiffness K of 0.1, 0.5, 1, 2, 5, and 50. The trailing edge amplitude A that normalized by the length L is calculated for different K, as defined in figure 6(a). The reduced stiffness is defined as $K = \frac{EI}{\rho_s \overline{U}_{tip}^2 L^3}$. The results of our simulation are shown in figure 6 which are also compare with the ones from the other two studies. Our results show good alignment with the other two studies.

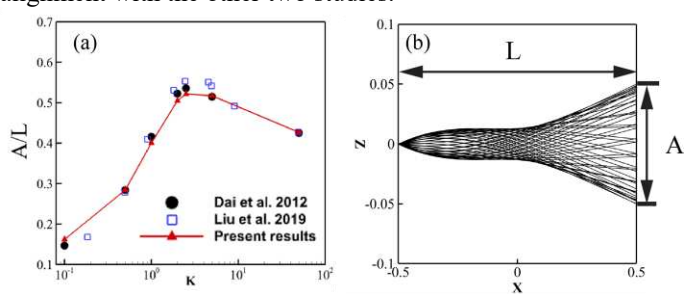


Figure 6. The comparison between the results from our solver and other studies, (b)The definition of the trailing edge amplitude.

2.7 Simulation setup

The reconstructed model is placed at the bottom a non-uniform Cartesian grid, where the flow domain has the dimension of $50 \times 15 \times 20$ (figure 7). The total grid size is 0.69 million cells and has $48 \times 8 \times 32$ cells. There is a denser mesh layer ($48 \times 8 \times 32$) right around the model at the bottom and a less dense mesh layer wrapping the denser mesh region. The exterior layers of mesh are stretched from the secondary layer to the boundary of the domain. The bottom boundary is non-slip, and the rest of the boundaries are set to zero-gradient boundary conditions.

The above mesh is for the simulation using only a single appendage (ctene). To investigate the effect of the interaction among multiple ctenes, cases with multiple ctenes are simulated, which require more meshes in x-direction. Therefore, for those cases, only the mesh in the dense region is extended by adding more mesh in x-direction while remains the same mesh density (dx). For 5-ctene case, denser mesh has $128 \times 8 \times 32$ cells.

In all the simulations, the Reynolds number $(Re = \overline{U}_{tip}L/v)$ is 50. The Poisson's ratio (v_s) is 0.25. The mass ratio $(m^* = \rho_s h/\rho_f L)$ is 0.1. The reduced stiffness $(K = EI/\rho_s \overline{U}_{tip}^2 L^3)$ is

0.65. The young's modules EI is set to 1.75×10⁸ which is a close value that can mimic the nature deformation of ctenophore's ctenes.

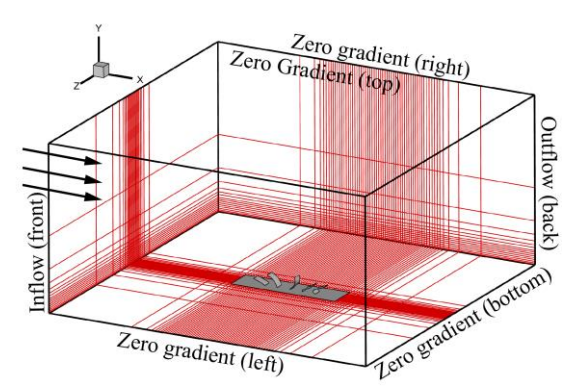


Figure 7. Boundary conditions of the simulation and the illustration of the computational grids.

2.7 Evaluation of hydrodynamic performance and nondimensionalization

By solving the Navier-Stokes equations, the surface pressure and the shear stress are computed, which can be used to calculate the hydrodynamic forces on each ctene. To evaluate the overall hydrodynamic performance, we calculated the individual ctene thrust coefficients. Here, the thrust and lift coefficients (C_{τ} and C_{ι}) are obtained from the horizontal and vertical forces along the inflow and given by equation (4) and (5).

$$C_{T} = \frac{F_{T}}{\frac{1}{2} \rho \bar{U}_{iip}^{2} S}; \tag{4}$$

$$C_{L} = \frac{F_{L}}{\frac{1}{2}\rho \overline{U}_{iip}^{2} S} \tag{5}$$

where ρ is the water density, $\overline{U}_{_{np}}$ is the mean ctene tip velocity averaged over one cycle, and S is the surface area of each comb plate.

The hydrodynamic power is calculated as the surface integral of the product of the pressure and velocity at each surface element, which is defined by equation (6). The power coefficient is given by equation (7) and the efficiency is defined by equation (8).

$$P = -\iint p\mathbf{n} \cdot \mathbf{u}_c ds \tag{6}$$

$$C_{p} = \frac{P}{\frac{1}{2}\rho \overline{U}_{np}^{3} S} \tag{7}$$

$$\eta = \frac{C_T}{C_B} \tag{8}$$

where u_c is the cell-centered velocity vector and n is the unit vector that is normal to the surface of the cell area ds.

3. RESULTS AND DISCUSSIONS

As Reynolds number is 50, it is believed that an temporal symmetrical beating is not capable of generating thrust [7,9]. Thus, to reproduce this through our FSI solver, the first simulation is conducted by using a temporally symmetrical beating model, which has Ta of 0. After 8 cycles, the resulting model deformation is shown in figure 8(a). The tip trajectory during the power stroke is similar to that during the recovery stroke. The cycle-averaged thrust coefficient is -0.86 indicating a non-effective propulsion from a symmetrical beating. The isosurface based on Q-criterion is shown in figure 9 for four instants. During the power stroke a tip vortex is formed along the tip edge of the ctene and disappear till the recovery stroke.

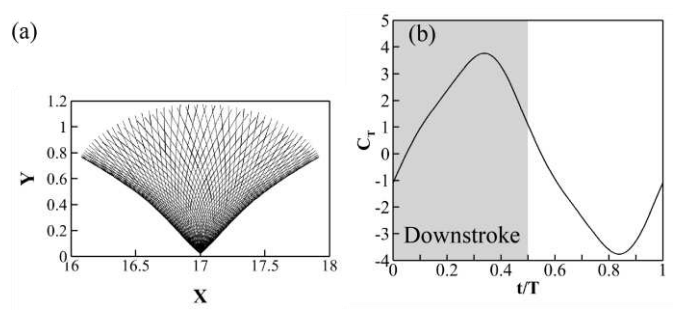


Figure 8. (a) The resulting model of the baseline case from the side view. (b) The time history of C_T over one cycle.

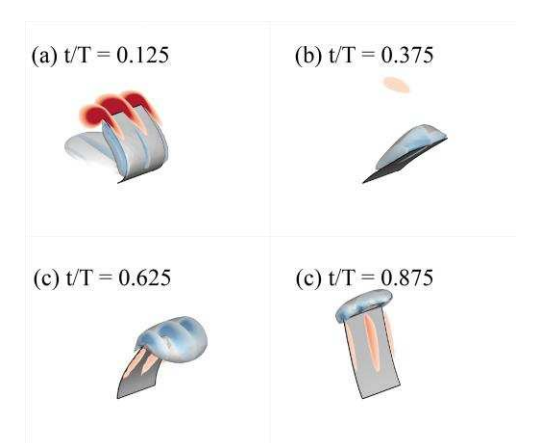


Figure 9. Isosurface of Q criterion and chordwise vorticity at t/T = 0.125, 0.375, 0.625, and 0.875.

Although our FSI solver also indicates that symmetrical beating cannot generate effective thrust, it is unclear how much the asymmetry is to produce the highest performance. Moreover, it is unknown whether there is an optimized asymmetry. Based on equation 1, the extent of the asymmetry of the beating can be easily examined by comparing the results of different asymmetry parameter Ta. Four additional cases with Ta = 0.2, 0.4, 0.6, and 0.8 are simulated under the same flow setup and material properties.

To compare the four cases with the baseline case, the according results are shown in figure 8(a). As Ta increases from 0 to 0.8, the power stroke period decreases accordingly, which indicates a higher acceleration. The peak and valley C_T are also achieved earlier. To find out which Ta has the best performance, we calculated cycle-averaged thrust $\overline{C_T}$ and plotted the $\overline{C_T}$ over Ta in figure 8(b). The optimal Ta for thrust generation is 0.4. The cases with Ta of 0.2 and 0.6 also can produce effective propulsion. But when Ta is too extreme as Ta = 0.8, the stroke also cannot generate positive net thrust.

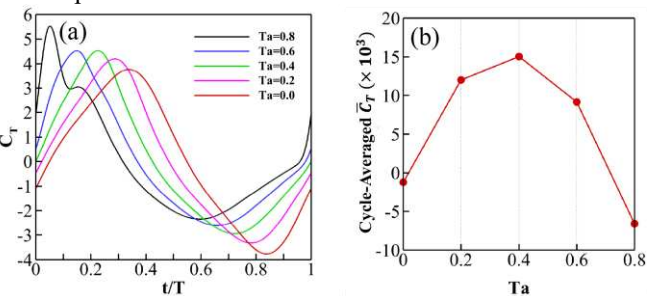


Figure 10. (a) The time history of C_T over one cycle for Ta = 0.0 (baseline), 0.2, 0.4, 0.6, 0.8.

To investigate what else parameter can make negative thrust due to the asymmetrical beating to positive thrust, we simulated cases with multiple ctenes. When multiple ctenes beating cooperatively, interactions among ctenes can potentially affect the thrust performance. But it is unclear if the influence is an enhancement. Our strong coupled FSI solver is suitable to solve this complex interaction problem.

Therefore, we have run the simulation with 5 ctenes in a row where the spacing is 3.5. The results of C_T is shown in figure 11. The cycle-averaged of mean C_T over 5 ctenes is 0.118. The thrust has been significantly improved compared to C_T of -0.86 in the baseline case.

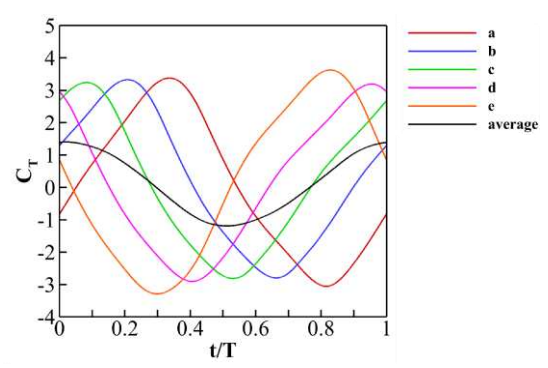


Figure 11. Time history of C_T and the mean C_T of 5 ctenes.

According to the results of the effects of Ta, there is an optimal Ta and a range of Ta values that benefits thrust generation. It is possible that this rule applies to the case with multiple ctenes. Therefore, we have conducted four more cases with different Ta as before but with 5 ctenes. The results of C_T are reported in form of mean C_T of the 5 ctenes. Figure 12(a) presents the time history of C_T generated by the ctene row under different asymmetry parameter Ta. From Ta of 0 to 0.6, similarly to the previous observation of single ctene cases, the C_T history has phase shift. The results with Ta under 0.8 show large numerical oscillations which is caused by the collision among ctenes due to phase lags. The collision should be ignored by the current stage of the study.

To summarize the relationship between the overall performance C_T of 5-ctene cases and the Ta, we have calculated the cycle-averaged C_T for different Ta (figure 12(b)). Similarly, Ta of 0.4 has the best performance. The range of effectively producing propulsion is extended to Ta of 0 instead of 0.2 for the single ctene case. Figure 12(b) compares 5-ctene cases with single ctene cases. Under Ta of 0.2 to 0.6, the thrust performance of 5-ctene cases outperforms the single ctene cases by 9 to 13 times.

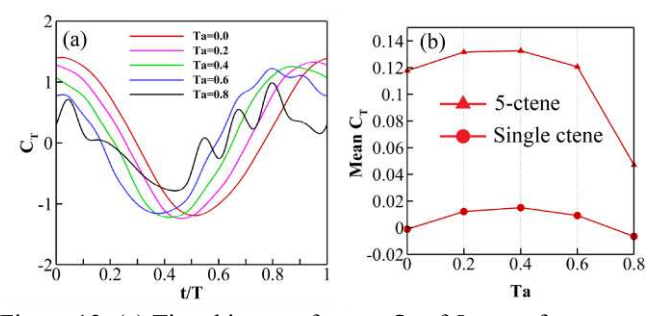


Figure 12. (a) Time history of mean C_T of 5 ctene for Ta = 0.0 (baseline), 0.2, 0.4, 0.6, 0.8. (b) the cycle average value of mean C_T of 5 ctenes for the single ctene cases and the 5-ctene cases versus Ta.

CONCLUSIONS

In our study, we have integrated our in-house computational fluid dynamics (CFD) solver with a finite element method (FEM) solver to solve fluid structure interaction problems. Convergence is achieved by strong coupling methods to generate more accurate solutions. We have run the simulations based on the model of a flat plate with several variation of parameters: Ta and number of total ctene.

Our investigation suggests that while symmetrical beating (Ta=0) can only generate negative net thrust, a slightly asymmetrical beating can make the thrust positive. As Ta ranges from 0.2 to 0.6, the thrust is effective compared with that with Ta of 0. We find that power stroke period that cost 30% whole period (Ta=0.4) can generates the highest thrust. We have also conducted the simulations while multiple ctenes stroke collaboratively to investigate the effect of interaction among multiple ctenes. As multiple ctenes involves, the interaction among ctenes can amplified the effects of the asymmetrical beating, so that the thrust generation is enhanced by 9 to 13 times because of it. Multiple ctene cases also show the same pattern that the Ta of 0.2 to 0.6 have the relatively good thrust performance while Ta of 0.4 performs the best.

ACKNOWLEDGMENTS

This research was supported by the National Science Foundation to C. Li (NSF CBET-2120505) and to M. L. Byron (NSF CBET-2120689). All simulations were run on the High-Performance Computing Cluster of the College of Engineering at Villanova University.

REFERENCES

- (1) Byron, M. L., Murphy, D. W., Katija, K., Hoover, A. P., Daniels, J., Garayev, K., Takagi, D., Kanso, E., Gemmell, B. J., Ruszczyk, M., and Santhanakrishnan, A. (2021) "Metachronal Motion across Scales: Current Challenges and Future Directions." Integrative and comparative biology, 61, 1674–1688.
- (2) Byron, M., Santhanakrishnan, A., and Murphy, D. (2021) "Metachronal Coordination of Multiple Appendages for Swimming and Pumping." Integrative and comparative biology, **61**, 1561–1566.
- (3) Chateau, S., Favier, J., Poncet, S., and D'Ortona, U. (2019) "Why Antiplectic Metachronal Cilia Waves Are Optimal to Transport Bronchial Mucus." Physical Review E, 100, 1–9.
- (4) Han, J., and Peskin, C. S. (2018) "Spontaneous Oscillation and Fluid–Structure Interaction of Cilia." Proceedings of the National Academy of Sciences of the United States of America, 115, 4417–4422.
- (5) Purcell, E. M. (1977) "Life at Low Reynolds Number." American Journal of Physics, **45**, 3–11.
- (6) Takagi, D. (2015) "Swimming with Stiff Legs at Low Reynolds Number." Physical Review E - Statistical,

- Nonlinear, and Soft Matter Physics, 92, 1–7.
- (7) Herrera-Amaya, A., Seber, E. K., Murphy, D. W., Patry, W. L., Knowles, T. S., Bubel, M. M., Maas, A. E., and Byron, M. L. (2021) "Spatiotemporal Asymmetry in Metachronal Rowing at Intermediate Reynolds Numbers." Integrative and comparative biology, 61, 1579–1593.
- (8) Gauger, E. M., Downton, M. T., and Stark, H. (2009) "Fluid Transport at Low Reynolds Number with Magnetically Actuated Artificial Cilia." European Physical Journal E, 28, 231–242.
- (9) Lou, Z., Adrian, H.-A., Byron, M. L., and Li, C. (2022) Hydrodynamics of Metachronal Motion: Effects of Spatial Asymmetry on the Flow Interaction Between Adjacent Appendages.
- (10) Sin, F. S., Schroeder, D., and Barbič, J. (2013) "Vega: Non-Linear FEM Deformable Object Simulator." Computer Graphics Forum, 32, 36–48.
- (11) Wang, J., Deng, X., Lauder, G. V., and Dong, H. (2019) "Numerical Investigation on Hydrodynamic Performance of Flapping Plates with Non-Uniform Spanwise Flexibility Using Fluid Structure Interaction." AIAA Aviation 2019 Forum, 1–10.
- (12) Dai, H., Luo, H., de Sousa, P. J. S. A. F., and Doyle, J. F. (2012) "Thrust Performance of a Flexible Low-Aspect-Ratio Pitching Plate." Physics of Fluids, 24.
- (13) Liu, G., Geng, B., Zheng, X., Xue, Q., Dong, H., and Lauder, G. V. (2019) "An Image-Guided Computational Approach to Inversely Determine in Vivo Material Properties and Model Flow-Structure Interactions of Fish Fins." Journal of Computational Physics, 392, 578–593.